Advanced Powder Technology 37 (2026) 105403

Contents lists available at ScienceDirect

Advanced Powder Technology

journal homepage: www.elsevier.com/locate/apt

Original Research Paper

CFD–DEM simulation of powder flow in a continuous coaxial nozzle for laser metal deposition

Lorenzo Pedrolli **, Beatriz Achiaga, Alejandro Lopez *

Department of Mechanics, Design and Industrial Engineering, University of Deusto, Av.da de las Universidades 24, Bilbao 48007, Spain

ARTICLE INFO

Article history:
Received 28 April 2026
Received in revised form 8 July 2026
Accepted 29 July 2026
Available online 12 August 2026

Keywords:
Multiphase flow
CFD–DEM
Laser metal deposition
Continuous coaxial nozzle
Powder stream stability

ABSTRACT

This work presents a fully coupled Computational Fluid Dynamics and Discrete Element Method (CFD–DEM) simulation of powder transport in continuous coaxial Laser Metal Deposition (LMD) nozzles, implemented in Simcenter STAR-CCM+. The methodology integrates a Johnson–Kendall–Roberts (JKR) adhesive contact model via custom field functions to represent cohesive particle–wall interactions influencing residence times and temporal flow structure. A refined polyhedral mesh resolves internal channels and external jet regions while maintaining coupling stability, with physics including two-species gas mixing (argon/air), Gidaspow drag, Sommerfeld shear lift, and gravity. Validation at a representative operating point (3 L/min carrier gas, 15 L/min shielding flow, Rosin–Rammler size distribution, 4.5 g/min feed) yields spatial footprints, centerline peak acceleration of ~50 m/s^2, and a 19% exit mass-flow irregularity (2 ms moving average). The predicted mass-flow irregularity (19% vs. 16% experimental) and accelerations agree closely with measurements, confirming rebound-driven intermittency and azimuthal redistribution at distributor fins as the dominant unsteadiness sources. Conversely, the standoff underprediction (10.2 mm vs. 16 mm) is traced to unresolved exit gas expansion under the incompressible assumption and drag calibration for the particle-laden jet, defining concrete refinement priorities for predictive simulation.

1. Introduction

Directed Energy Deposition (DED) by Laser Metal Deposition (LMD) relies on the controlled delivery of a metal powder stream coaxial to the laser. Continuous coaxial nozzles are favored for their azimuthal symmetry and robustness against tooling direction changes, yet suffer from sensitivity to internal flow distribution and exit acceleration that govern powder capture efficiency. LMD is widely used for near-net-shape fabrication, repair, and functional coatings across alloys and multi-materials [1,2]. Powder feedstock handling, metering, and delivery have a direct impact on deposition quality and efficiency [3]. Among nozzle families, continuous coaxial nozzles are favored for symmetry, while discrete coaxial designs can enhance catchment for specific standoff and angle conditions [4,5].

In a continuous coaxial layout, two gas systems are typically distinguished: a conveying stream that entrains and accelerates powder from peripheral inlets and a shielding stream that protects the optics and interacts with the external jet. The distributor and converging sections must homogenize the azimuthal momentum to avoid lopsided focusing and off-axis footprints. Geometric tolerances, pressure losses across fins and turning chambers, and the ratio of shielding to conveying flow therefore play a central role in powder capture. Small deviations in the internal momentum balance can translate into millimeter-scale shifts in the focal plane and percent-level losses in powder utilization. In practice, operators tune the usable standoff window by adjusting the flow split and total gas rate, but this tuning is nozzle-specific and often empirical.

Design trade-offs are well known: continuous coaxial heads maximize directional robustness for multi-axis paths, while multi-jet (discrete) coaxial heads can deliver higher peak concentration at the focus for a narrower process window [4,5]. Across both families, the exit acceleration that the gas can impart to a polydisperse powder -together with jet stability and the degree of air entrainment- ultimately governs the stream convergence and the usable catchment with the laser. Understanding these mechanisms quantitatively, and how they respond to geometry and operating point, motivates detailed simulation supported by experiments [6].

* Corresponding author.
** Corresponding author.
E-mail addresses: l.pedrolli@deusto.es (L. Pedrolli), alejandro.lopez@deusto.es (A. Lopez).

https://doi.org/10.1016/j.apt.2026.105403
0921-8831/

Powder-stream modelling typically couples the gas phase with particle transport using Eulerian–Lagrangian approaches or Eulerian-Eulerian alternatives. Recent works report accurate predictions of powder cone geometry and focal-plane concentration maps for three- and four-way nozzles, with k–ω Shear Stress Transport (SST) often selected for internal jets and separation [7,8]. Earlier continuous-coaxial studies used one-way coupling to estimate powder footprints at the focus [6]. Guan et.al. summarize powder-laser interactions and parameter sensitivities [9]. More recent studies have extended nozzle powder-flow simulation in several directions: Gao et al. analyzed the influence of nozzle geometry on powder flow behaviors in DED, highlighting the sensitivity of stream convergence to internal channel design [10]; Mukin et al. modeled the gas–powder jet formed by a single nozzle tube in direct laser deposition, combining analytical jet theory with particle tracking validated against optical measurements [11]; Qin et al. characterized the spatial dynamic behavior of the powder stream and individual particles during coaxial laser cladding [12]; and Zhang et al. demonstrated active particle motion control by ultrasonic fields in DED, illustrating the growing interest in manipulating the powder stream downstream of the nozzle [13]. These works confirm a trend toward higher-fidelity, experimentally anchored models of the powder stream, yet they largely treat particle–wall interactions with simplified contact assumptions and rarely report the temporal stability of the delivered mass flow.

In dispersed multiphase simulation, point-particle Euler–Lagrange with Reynolds-Averaged Navier–Stokes (RANS) turbulence remains prevalent for engineering analysis [14,15]. Gas–solid coupling depends on drag/lift closures; drag choice influences slip at the exit and thus standoff [16]. Multiphase Particle-In-Cell (MP-PIC) methods offer an Eulerian-Eulerian route for dense regimes and large domains [17,18], but do not capture temporal variability in pneumatic conveying [19]. Open questions include (i) compressibility effects on exit acceleration and drag [20], (ii) contact/adhesion influences on residence in distributor structures [21–23], and (iii) quantifying temporal irregularities of the powder stream [24].

Most nozzle-focused works treat particle contacts with walls in a simplified manner (purely elastic or with constant restitution). However, even weak cohesive effects and tangential friction at distributor fins can alter residence times, local seeding, and the temporal structure of the powder flow that emerges from the throat [22,23]. DEM-enhanced formulations (CFD–DEM) allow these mechanisms to be represented explicitly while reusing standard drag/lift closures [15]. The present work includes a lightweight adhesive contact model and extracts nozzle performance metrics directly from the transient solution. The influence of the contact treatment on the delivered powder flow is assessed in Section 3.3, where the temporal irregularity of the exit mass flow—driven by wall rebound and residence in the distributor—is quantified and compared with experiments.

This paper focuses on the simulation aspects of a continuous coaxial nozzle. First, we aim to assemble a STAR-CCM + setup tailored to continuous coaxial heads that combines polyhedral meshing, RANS k–ω SST, and a Lagrangian particulate solver with DEM contact augmented by a JKR-type adhesion term, targeting robustness for long transients. Second, we aim to define process-relevant metrics that can be computed automatically from the flow solution: standoff distance from percentile-based focusing, linear and radial footprint widths at the focal plane, particle acceleration/velocity evolution along the centerline, and an irregularity index for exit mass flow. Third, we compare the simulated trends with a companion experimental dataset [24] to identify modeling gaps—notably exit compressibility and drag calibration—and to outline a practical path toward predictive calibration for nozzle tuning. The companion study [24] documents the full experimental campaign (high-speed imaging of the powder stream, standoff and footprint measurements, and time-resolved mass-flow estimation) on the same nozzle and at the same operating point simulated here; the present validation is therefore intentionally restricted to that single, fully characterized operating condition, and extension to additional flow rates and geometries is planned as future work.

The present work makes three methodological contributions to multiphase simulation practice: **(i)** Integration of a JKR adhesive contact model within a commercial CFD–DEM solver via custom field functions, demonstrating how production tools can be extended for cohesive particulate flows without source-code modification; **(ii)** A systematic framework for extracting process-relevant metrics from transient particle fields that can be automated for parametric studies and nozzle optimization campaigns; and **(iii)** Transparent documentation of modeling assumptions, verification procedures, and quantitative impact on predictions, enabling practitioners to assess applicability to their own systems and identify refinement priorities. These contributions advance the state of simulation practice for powder-based additive manufacturing by providing a validated, reproducible methodology with clear guidance on model limitations and improvement paths.

2. Methods

This section is organized following the structure of the coupled fluid–particle problem. SubSection 2.1 describes the computational domain and mesh. SubSection 2.2 presents the governing equations: the Eulerian gas-phase (fluid) equations first, then the Lagrangian particle-phase (solid) equations with DEM contact, and finally the interphase data transfer (two-way momentum coupling) and time-integration scheme. SubSections 2.5–2.7 detail the boundary and injection conditions, near-wall treatment, and the adhesive contact model, and SubSection 2.8 defines the post-processing metrics.

2.1. Geometry and mesh

The computational domain comprises the internal channels (four conveying inlets, lens shielding inlets, distributor fins, converging throat) and an external cylindrical region for the free jet. Fig. 1 shows a half-sectioned view of the nozzle with annotations of the main features used in the simulations. It provides a clear view of the internal structure: the annulus between the internal cone and the outer walls forms the powder channel. A vertical-channel distributor in the middle section has the objective to homogenize azimuthal momentum and suppress swirl. The high-power laser travels through the central channel, protected by a continuous argon shielding stream; the focusing lens is mounted at the top of the channel. The measurements are in mm, starting from the bottom face of the nozzle (z = 0 mm) up to the top face, for a total height of the simulation domain of 138 mm.

A polyhedral mesh was generated in STAR-CCM + with targeted refinements in: (i) distributor channels, (ii) cone-to-throat annulus, and (iii) exit region. The final mesh counts $\sim$4.1 million cells, with $> 99\%$ polyhedra. Cell volumes range from 1.1×10^{-14} to 3.5×10^{-9} m^3, chosen to avoid parcels larger than the smallest cells and to maintain stable two-way coupling.

Polyhedral elements provide superior adaptability and robustness compared to purely tetrahedral meshes in complex, slender passages; their convex angles reduce distortion-induced errors and they often converge faster for a given accuracy target. Literature reports polyhedra as a strong alternative to hexahedra in respiratory aerosol transport, which is analogous in terms of slender passages and recirculation pockets [25]. In the present case, the polyhedral mesh enabled stable DEM coupling without excessive cell count or distortion issues, while allowing for cells larger than the parcels [19].

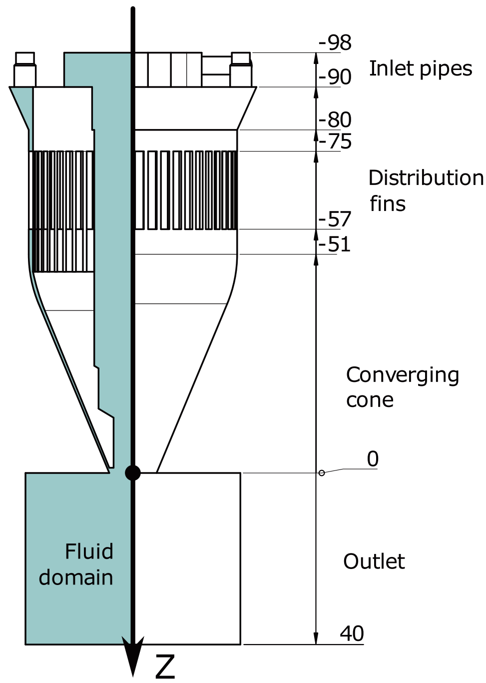

Fig. 1. Half-sectioned view of the continuous coaxial nozzle geometry with key features annotated. The internal cone, distributor fins, conveying inlets, and shielding inlets are visible, along with the external cylindrical domain for the free jet. The main nozzle axiz Z is indicated, dimensions are in mm.

The mesh must balance detail and computational efficiency, ensuring that critical regions, such as the nozzle exit, are sufficiently refined to capture important flow characteristics. Using the provided geometry of the fluid domain, the mesh was generated using the advanced tools in STAR-CCM+. Gradual refinement levels were defined in the critical regions:

- in the small distributor channels;
- in the small space between the cone walls;
- at the exit of the nozzle, where the flow transitions from a constrained to an open domain.

Fig. 2a provides an overview of the simulated nozzle's mesh, while Fig. 2b offers a detailed view of the refined mesh at the nozzle exit.

The final computational mesh consists of a total of 4102881 cells, with 4085818 being polyhedral cells, alongside a small number of tetrahedral, hexahedral, wedge, and pyramid cells necessary to adapt to the geometry; all face validity metrics are satisfied. The containing prism for the mesh is $57.5 \times 57.5 \times 138$mm in the x, y, and z directions respectively, with the origin placed at the center of the nozzle's bottom face. Cell volumes range from $1.09 \times 10^{-14}\text{m}^3$ to $3.50 \times 10^{-9}\text{m}^3$; for comparison, a spherical particle with a diameter of 100μm has a slightly smaller volume of approximately $5.24 \times 10^{-15}\text{m}^3$, so no parcel exceeds the smallest cells. A formal mesh-independence study across multiple resolutions was not performed owing to the cost of the coupled transient runs ($\sim$3000 core-hours per case, SubSection 2.4); mesh adequacy is instead supported by the refinement strategy targeting the highest-gradient regions, the mesh-quality metrics above, and the agreement of integral outputs with experiments. This is acknowledged as a limitation in SubSection 3.4.

2.2. Governing equations and coupling

We solve the incompressible, isothermal multi-component RANS system with an Eulerian gas phase and a Lagrangian particulate phase coupled via volume-averaged source terms. The formulation is presented in the order fluid phase → solid phase → interphase data transfer.

Fluid phase. The gas phase follows the standard continuity and momentum equations with turbulent viscosity from the SST k–ω model [26], which transports turbulent kinetic energy and specific dissipation to capture the adverse pressure gradients in the converging section. Species transport equations govern the mixing of argon (from inlets) and air (ambient), with mixture properties evaluated via mass-weighted combinations at 20°C and 1 atm. The incompressible assumption is justified a priori by the flow regime: with the prescribed volumetric flows (SubSection 2.5), the bulk gas velocity remains below $\sim$10 m/s in the supply pipes and reaches its maximum in the annular throat, where the local Mach number is estimated at $Ma \approx 0.1$–0.3. In the internal channels, where most of the particle-flow structure develops, $Ma < 0.1$ and density variations scale as $\Delta\rho/\rho \sim Ma^2 \lesssim 1\%$, which is negligible. Only in the immediate exit region does the upper bound $Ma \approx 0.3$ imply density variations up to $\sim$5–9%, so a locally reduced gas expansion (and hence particle acceleration) is expected; this is discussed quantitatively in relation to the standoff

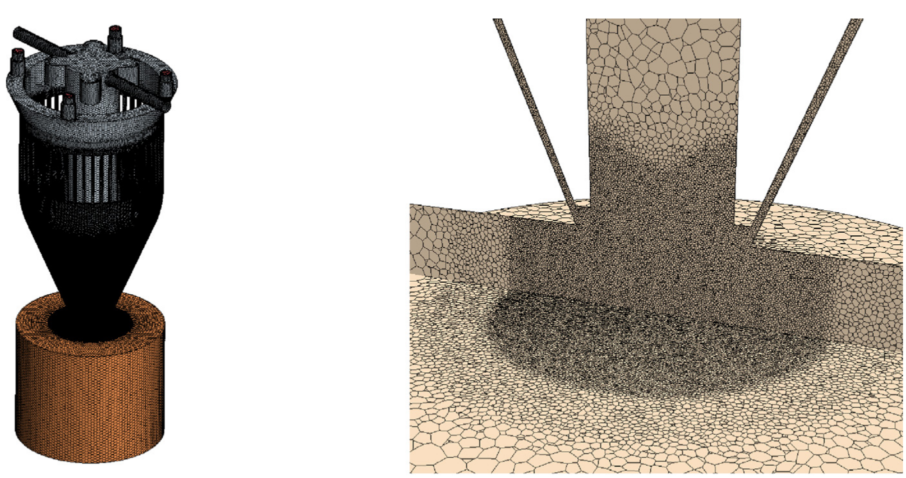

(a) (b)

Fig. 2. (a) Overview of the simulated nozzle's mesh. (b) Detailed view of the refined mesh at the nozzle exit.

prediction in SubSection 3.1 and listed as a refinement priority in SubSection 3.4.

Solid phase. The particle equation of motion for each parcel (index p, density ρ_p, diameter d_p) reads:

$$\frac{d\mathbf{x}_p}{dt} = \mathbf{v}_p, \tag{1}$$

$$\frac{d\mathbf{v}_p}{dt} = \frac{\mathbf{F}_{\text{drag}} + \mathbf{F}_{\text{lift}} + \mathbf{F}_{\text{g}} + \mathbf{F}_{\text{contact}}}{m_p}, \quad m_p = \frac{\pi}{6}\rho_p d_p^3. \tag{2}$$

Drag follows the Gidaspow model [27], which blends the Wen–Yu correlation for dilute flows ($\epsilon_g > 0.8$) with the Ergun equation for dense regimes ($\epsilon_g \leqslant 0.8$), using the gas volume fraction ϵ_g and particle Reynolds number $Re_p = \rho_g d_p \|\mathbf{u} - \mathbf{v}_p\|/\mu$:

$$\mathbf{F}_{\text{drag}} = \begin{cases} \frac{3}{4} C_D \frac{\rho_g}{\epsilon_g d_p} \|\mathbf{u} - \mathbf{v}_p\| (\mathbf{u} - \mathbf{v}_p)\, \epsilon_g^{-2.65} m_p & \text{if} \epsilon_g > 0.8, \\ 150 \frac{(1-\epsilon_g)^2 \mu}{\epsilon_g d_p^2} + 1.75 \frac{(1-\epsilon_g)\rho_g \|\mathbf{u}-\mathbf{v}_p\|}{d_p} \quad (\mathbf{u} - \mathbf{v}_p)\, \frac{V_p}{\epsilon_g} & \text{if} \epsilon_g \leqslant 0.8, \end{cases} \tag{3}$$

$$C_D = \frac{24}{Re_p}\left(1 + 0.15\, Re_p^{0.687}\right), \tag{4}$$

where $V_p = \pi d_p^3/6$ is the particle volume. Lift uses a Sommerfeld shear-induced formulation [15]. Particle contacts are resolved by DEM with a linear-viscoelastic basis extended by JKR-type adhesion to capture mild cohesion between metallic particles and walls (see subSection 2.7 and Appendix A for full model description and implementation). While the drag, lift, and blending correlations are empirical in origin, each is applied within its established validity envelope for the present regime: the particle Reynolds numbers encountered here ($Re_p \sim 1$–10^2) and the predominantly dilute volume fractions ($\epsilon_g > 0.95$ in most of the domain) fall inside the ranges for which the Wen–Yu/Schiller–Naumann branch of the Gidaspow correlation was derived, with the Ergun branch engaged only in transient near-wall accumulations at the distributor [27,15]. The applicability of the contact-model parameters is addressed separately in SubSection 2.7 and Appendix A.

Interphase data transfer. Momentum and species sources from particles are volumetrically distributed using the Cell Cluster smoothing with characteristic length $\ell_c = 350\,\mu$m to enhance stability while preserving locality. The coupling is two-way: the gas exerts drag and lift on the particles, and the equal-and-opposite reaction is accumulated per cell cluster and returned to the gas momentum equation at each coupling step.

Time integration. Gas phase uses the Pressure-Implicit with Splitting of Operators (PISO) algorithm with $\Delta t = 10^{-4}$ s. The Lagrangian integrator substeps to maintain local Courant $\leqslant 0.35$. DEM contact time step is set as $\Delta t_{\text{DEM}} = t_{\text{Rayleigh}}/5$, with Rayleigh time

$$t_{\text{Rayleigh}} = \pi R \sqrt{\frac{\rho_p}{G\eta}}, \tag{5}$$

for particle radius $R = d_p/2$, shear modulus G, and Poisson correction η.

2.3. Physics models and solvers

The physics selections summarized here complement the governing equations of SubSection 2.2; this subsection focuses on the rationale for each modeling choice and the material properties used.

Model selection rationale: The SST k–ω model was selected over standard k–ϵ because it better captures adverse pressure gradients in the converging section and provides superior near-wall performance without requiring fine prism layers [26]. The Gidaspow drag formulation was chosen for its ability to handle both dilute ($\epsilon_g > 0.8$) and moderately dense ($\epsilon_g \leqslant 0.8$) regimes through its Wen–Yu/Ergun blending, relevant near distributor fins where local particle concentrations can vary significantly [27]. Polyhedral meshing was preferred over hexahedral or tetrahedral alternatives because it provides superior adaptability in complex geometries with fewer cells, faster convergence, and reduced sensitivity to stretching—critical for maintaining DEM coupling stability [25]. The All-y^+ wall treatment eliminates the need for inflation layers that would create excessively small cells relative to particle sizes, trading detailed boundary-layer resolution for robust coupling at moderate computational cost.

Gas properties at reference conditions: Argon $\rho = 1.6339$ kg/m^3, $\mu = 2.2768 \times 10^{-5}$ Pa s; Air $\rho = 1.1842$ kg/m^3, $\mu = 1.8551 \times 10^{-5}$ Pa s. The transient simulation is started from a steady, gas-only initialization before particle injection is activated.

2.4. Computational environment and cost

Hardware and software: Simulations were performed on a dual-processor workstation (2× Intel Xeon E5-2620 v4, 64 GB RAM) running windows 11, using Simcenter STAR-CCM + version 2406. The solver was executed in parallel using 14 cores with domain decomposition.

Computational cost: Each global time step (with Lagrangian substepping and DEM contact) required approximately 40 s of wall-clock time, equivalent to 560 core-hours per second of physical time. For ~2 s of physical time following initial transients, the overall cost amounted to roughly 220 h wall-clock time (3080 core-hours). While expensive, this setup allowed extraction of converged statistics for stream focusing, acceleration, and exit mass-flow irregularities. The cost scales approximately linearly with the number of particles and mesh cell count for the dilute regime encountered here ($\epsilon_g > 0.95$ in most of the domain).

2.5. Boundary and injection conditions

At the outer boundary, we apply a pressure outlet of 1 atm on the external cylinder and allow backflow along the boundary normal. All walls are no-slip with turbulence wall functions. The shielding gas enters through two velocity inlets that carry a total of 15 L/min via 4.2 mm pipes. The conveying gas enters through four velocity inlets that carry 3 L/min in total, also via 4.2 mm pipes. Powder is injected from the conveying inlets as a random surface source at a constant 4.5 g/min, with a Rosin–Rammler PSD spanning 40–180 μm. The domain is initialized with Air ($Y_{\text{Air}} = 1$); all inlets prescribe Argon ($Y_{\text{Ar}} = 1$), and mixing proceeds via the species-transport equations using an effective Schmidt number.

To make the inlet settings explicit, we convert volumetric flow to speed using $U = Q/A$ (per pipe). All inlet pipes have a circular cross-section of diameter $D = 4.2$ mm $\Rightarrow$ area $A = \pi(D/2)^2 = 1.385 \times 10^{-5}$ m^2.

- Shielding inlets (2 pipes, total $Q = 15$ L/min $= 2.5 \times 10^{-4}$ m^3/s): $Q_{\text{pipe}} = 1.25 \times 10^{-4}$ m^3/s $\Rightarrow U \approx 9.0$ m/s (applied to each shielding pipe).
- Conveying inlets (4 pipes, total $Q = 3$ L/min $= 5.0 \times 10^{-5}$ m^3/s): $Q_{\text{pipe}} = 1.25 \times 10^{-5}$ m^3/s $\Rightarrow U \approx 0.90$ m/s (applied to each conveying pipe).

The powder total mass flow is fed in equal proportions through the conveying inlets: $\dot{m}_p = 4.5$ g/min $= 7.5 \times 10^{-5}$ kg/s, split evenly among the four conveying pipes $\Rightarrow \dot{m}_{p,\text{pipe}} = 1.875 \times 10^{-5}$ kg/s each.

We characterize the powder size statistics with a Rosin–Rammler (Weibull-type) cumulative distribution, commonly used for atomized metallic powders because it captures a rapid rise in fine fractions followed by a long tail of coarse particles. The cumulative passing fraction for size d is

$$R(d) = 1 - \exp\left[-\left(\frac{d}{d_0}\right)^n\right], \tag{6}$$

where d_0 is a characteristic scale (roughly the size at which $R \approx 0.63$) and n controls the steepness of the curve (higher n yields a tighter distribution). The experimental powder, characterized by optical image analysis [28] and SEM image binarization [19], is well fitted by $d_0 = 63.65\,\mu$m and $n = 5.177$. We truncate that theoretical curve to the physically observed bounds $[40, 110]\,\mu$m to remove extremely rare fines and coarse outliers that would add negligible mass yet increase computational cost.

For the present simulation campaign we intentionally adopt a simplified, coarser PSD ($d_0 = 120\,\mu$m, $n = 10$, truncated to $[80, 150]\,\mu$m). This adjustment reduces the number of very small particles that would demand tighter DEM and coupling time steps, while still spanning the dominant momentum-carrying sizes relevant for jet focusing. All quantitative results reported below refer to this simulation-time PSD unless explicitly stated; where trends are discussed qualitatively (e.g., sensitivity of standoff to drag) they are consistent with the experimentally fitted, finer distribution.

The implications of this simplification can be bounded from the particle equation of motion. The particle aerodynamic response time in the Stokes limit scales as $\tau_p = \rho_p d_p^2/(18\mu)$, so shifting the mass-median diameter from $\approx 64\,\mu$m to $\approx 120\,\mu$m increases τ_p by a factor of $\sim$3.5. Coarser particles are therefore less responsive to the gas acceleration at the exit and to turbulent dispersion: the simulated stream is expected to exhibit (i) a slightly lower exit velocity gain for a given gas expansion, contributing to the standoff underprediction, and (ii) a narrower dispersion halo, since the omitted sub-80 μm fraction is the most susceptible to lateral turbulent transport and to adhesive wall interactions. Conversely, the exit mass-flow irregularity metric is dominated by rebound events and azimuthal redistribution of the momentum-carrying (coarse) fraction, and is therefore expected to be less sensitive to the removal of fines — consistent with the close agreement obtained for that metric (Section 3.3). A comparative simulation with the experimentally fitted PSD was not affordable within the present computational budget (the finer sizes reduce both the DEM and coupling time steps, multiplying the cost) and is identified as a priority for follow-up work in SubSection 3.4.

2.6. Near-wall treatment

No prism (inflation) layers were used at walls to maintain numerical stability with DEM coupling and to avoid excessively small near-wall cells relative to the largest parcels. The SST k–ω model with All-y^+ treatment was selected accordingly. Given the fine near-wall cell sizes from the polyhedral mesh, the effective y^+ remained within the model's acceptable range across the internal channels and the exit region. This choice trades detailed wall-shear resolution for solver robustness while preserving integral jet behavior and exit acceleration central to the present study.

2.7. JKR contact model

To represent mild cohesion between metallic particles and walls, we implemented a Johnson–Kendall–Roberts (JKR) adhesive. The elastic contact model within the STAR-CCM + DEM framework via field functions. The adhesive normal force augments the Hertzian term with a surface-energy contribution, producing the characteristic hysteresis between approach and separation. In terms of the effective modulus E^*, reduced radius R^*, and instantaneous contact radius a, the normal component reads

$$\mathbf{F}_N = -\left[\underbrace{\frac{4E^*a^3}{3R^*}}_{\text{Hertz}} - \underbrace{\sqrt{8\pi\Gamma_{12}E^*a^3}}_{\text{JKRadhesion}}\right]\hat{\mathbf{n}} - c_n\,(\mathbf{v}_{\text{rel}}\cdot\hat{\mathbf{n}})\,\hat{\mathbf{n}}, \tag{7}$$

with surface energy Γ_{12}, contact normal $\hat{\mathbf{n}}$, and relative velocity $\mathbf{v}_{\text{rel}}$. The effective elastic properties are

$$E^* = \left[\frac{1-\nu_0^2}{E_0} + \frac{1-\nu_1^2}{E_1}\right]^{-1}, \tag{8}$$

$$G^* = \left[\frac{2(1+\nu_0)(2-\nu_0)}{E_0} + \frac{2(1+\nu_1)(2-\nu_1)}{E_1}\right]^{-1}, \tag{9}$$

$$\frac{1}{R^*} = \frac{1}{R_0} + \frac{1}{R_1}, \tag{10}$$

and the equilibrium (adhesive) contact radius is

$$a_0 = \left(\frac{9\pi\Gamma_{12}R^{*2}}{2E^*}\right)^{1/3}. \tag{11}$$

The tangential force uses a Mindlin-like spring with dashpot and a Coulomb cap,

$$\mathbf{F}_T = \mathbf{F}_{T,\text{Mindlin}}\ \text{cappedby}\ \|\mathbf{F}_T\| \leqslant \mu\,\|\mathbf{F}_N\|, \tag{12}$$

$$\mathbf{F}_{T,\text{Mindlin}} = -k_t\,\boldsymbol{\delta}_t + c_t\,\mathbf{v}_t, \qquad k_t \propto G^*\sqrt{R^*\,\delta_n}, \tag{13}$$

with friction coefficient μ, tangential overlap $\boldsymbol{\delta}_t$, and tangential slip velocity $\mathbf{v}_t$. Normal and tangential damping are set from the desired normal restitution e via the standard coefficient

$$\beta = \frac{\ln e}{\sqrt{(\ln e)^2 + \pi^2}}, \qquad c_n \propto \beta\sqrt{k_n m^*}, \qquad c_t \propto \beta\sqrt{k_t m^*}, \tag{14}$$

with reduced mass m^*. Hysteresis is enforced by activating adhesion once the contact radius exceeds a formation threshold $a_{\text{form}} = (2/3)^{2/3}a_0 \approx 0.76\,a_0$ on approach [29], and allowing tensile "pull-off" until $a \to 0$ on separation; this yields the expected asymmetric, non-conservative work loop for adhesive elastic contacts.

In the StarCCM + field function implementation, the driving variable for the contact is the contact radius a, as opposed to the more common overlap-based formulation δ_n. This choice simplifies the detection of the adhesion onset and pull-off conditions, as a is directly available in StarCCM, and allows to leverage the existing DEM contact framework with minimal modifications. The contact radius is computed internally by STAR-CCM + based on the geometry of the contacting bodies and their relative positions, ensuring accurate representation of the contact mechanics. The downside is tha the force-overlap relationship is shifted to be completely inside the contact radius domain, but this small difference is acceptable for the intended application.

In this study we used $\mu = 0.62, \Gamma_{12} = 0.01$ J/m^2, and normal restitution $e = 0.9$. These values are not arbitrary: the surface energy $\Gamma_{12} = 0.01$ J/m^2 was estimated for the same class of gas-atomized stainless-steel powder by the kinetic adhesion test methodology developed by our group [30], which back-computes the mesoscale surface energy from measured detachment velocities and lies within the range reported for lightly oxidized metallic powders [21,23]. The restitution coefficient $e = 0.9$ is consistent with the impact measurements of Odum et al. on metallic powder rebound from DED nozzle materials [31] and with values commonly adopted for hard metallic microparticles [22]. The friction coefficient $\mu = 0.62$ corresponds to steel-on-steel dry sliding and follows established DEM calibration practice for cohesionless bulk metals [32,33]. Qualitatively, these parameters act on distinct observables: Γ_{12} chiefly affects residence times near fins and walls (adhesion delays re-entrainment of slow particles), e controls the energy retained in wall rebounds and hence the rebound-driven intermittency of the exit flow, and μ bounds lateral momentum exchange during oblique impacts. The single-particle verification of the implemented contact law, including the force–displacement hysteresis loop and the energy dissipated per impact, is reported in Appendix A (Fig. A.7).

2.8. Post-processing metrics

From the transient fields we compute: (i) standoff distance as the axial location of minimum diameter enclosing 90% of particles; (ii) stream width at standoff from the 50/90/99th percentiles of radial and linear (X) distributions; (iii) particle axial velocity and median acceleration along z; and (iv) exit powder mass flow with 2 ms moving-average RMS.

3. Results and discussion

3.1. Stream convergence and standoff

Fig. 3 shows the time-averaged side view of the particle probability density, with percentile bands. The simulated standoff distance is 10.2 mm from the exit, lower than the experimental estimate (16 mm, [24]). We attribute the difference primarily to lower predicted exit particle velocity due to limited gas expansion in the incompressible RANS setup and potential drag underestimation in the shear layer.

The plausibility of these two contributions can be assessed with a simple ballistic estimate. For a particle leaving the nozzle annulus with axial velocity v_z and radial convergence angle θ set by the exit cone, the geometric focus lies at $z_f \approx r_{\text{exit}}/\tan\theta$ measured along the axis; the effective standoff additionally grows with the ratio of particle inertia to the decelerating/entraining action of the ambient jet. Because the convergence angle is fixed by the nozzle geometry, the standoff is mainly sensitive to how long the particles preserve their exit momentum. A locally compressible gas expansion at the exit (with $Ma \approx 0.1$–0.3, corresponding to density variations up to $\sim$9%) would increase the gas exit velocity—and thus the particle velocity at the focus—by up to a comparable fraction; combined with the coarser simulated PSD, whose response time is $\sim 3.5\times$ longer than the experimental one (SubSection 2.5), the two effects act in the same direction and are consistent with the observed $\sim$36% underprediction. Isolating and quantifying each contribution requires a compressible exit-region model and a PSD-matched rerun, both of which exceed the present computational budget and are deferred to future work.

Method: the particle distribution is accumulated over time on x–z bins; at each axial position z, we compute the smallest diameter enclosing 90% of particles (P90). The standoff is the z yielding the minimum of this P90 diameter. Horizontal markers in Fig. 3 denote the ± 0.5 mm slice used around the identified standoff plane for footprint statistics. Sensitivities: the P90-based standoff is robust to outliers; it varies < 0.5 mm when the bin size is halved and ≈ 1 mm when P90 is replaced by P80/P95.

3.2. Velocity and acceleration along the nozzle

Particles exhibit broad directional dispersion near the inlets, followed by alignment in the converging section. A sharp acceleration peak (≈ 53 m/s^2) occurs near the throat and exit (Fig. 4), matching the order of magnitude inferred from experiments [24] and supporting the adequacy of the chosen drag model. At the exit, particles confined within the nozzle by the conveying gas encounter the higher-velocity shielding stream and experience rapid expansion into ambient pressure, gaining significant momentum critical for achieving the desired standoff and focusing characteristics. The simulation underrepresents this acceleration due to the incompressible RANS assumption, which limits gas expansion and consequently constrains the predicted exit velocity and standoff distance. (see Fig. 5).

Additional observations: rebounds upstream of the distributor lead to a wide velocity spread that tightens through the fins. A secondary acceleration feature is observed near $z \approx -70$ mm at the fin entrance, followed by deceleration at the exit of the fin channels, indicating energy exchange with the gas shear.

These features admit a consistent mechanistic reading of how the internal components shape the powder stream. Upstream of

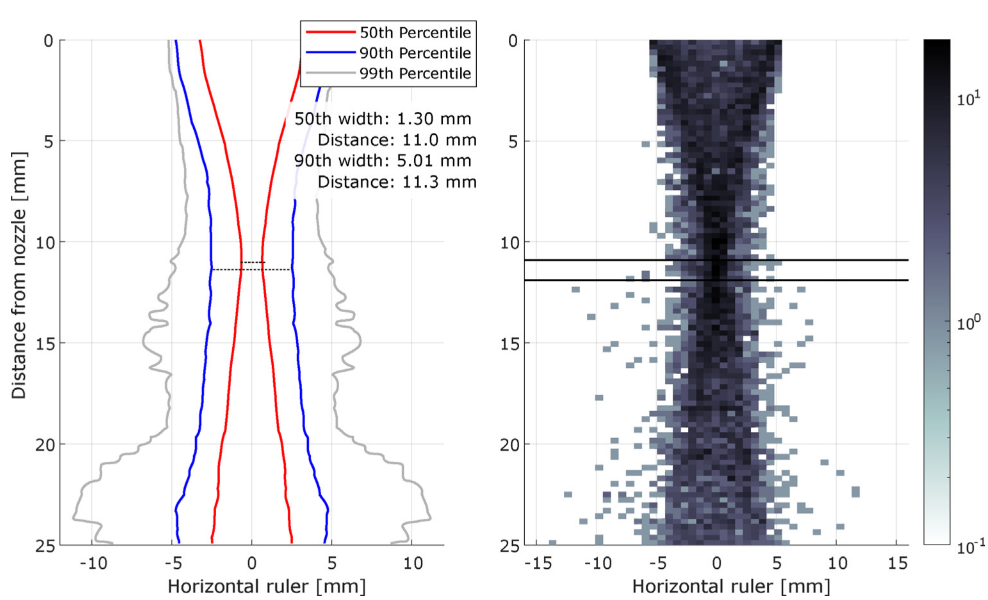

Fig. 3. Side view of simulated particle distribution and percentiles; horizontal markers indicate a 1 mm slice around the standoff distance.

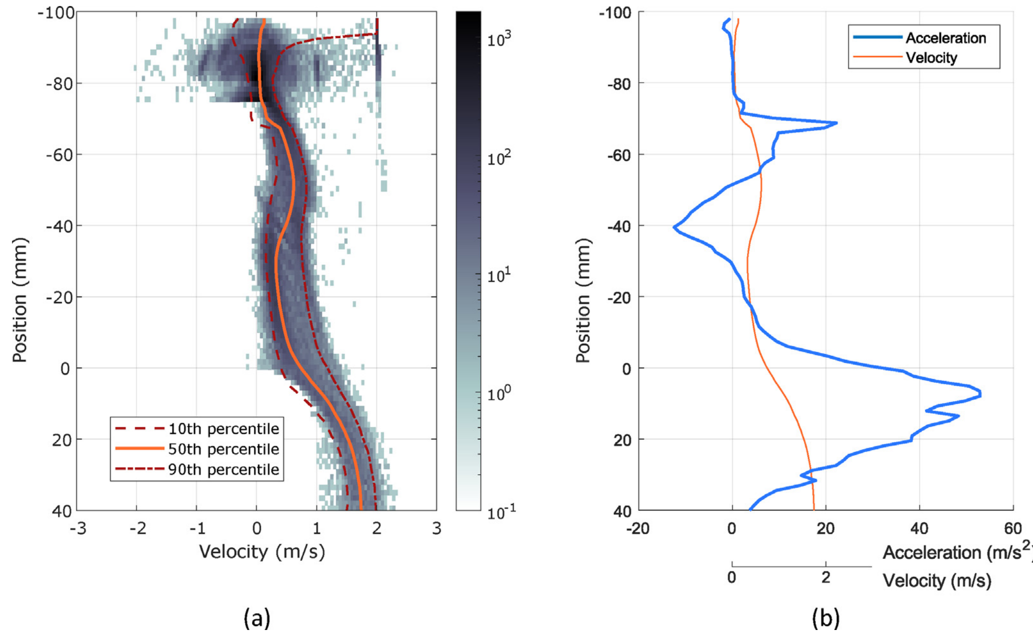

Fig. 4. Axial particle velocity percentiles and median acceleration along the axis of the nozzle *Z*, see Fig. 1.

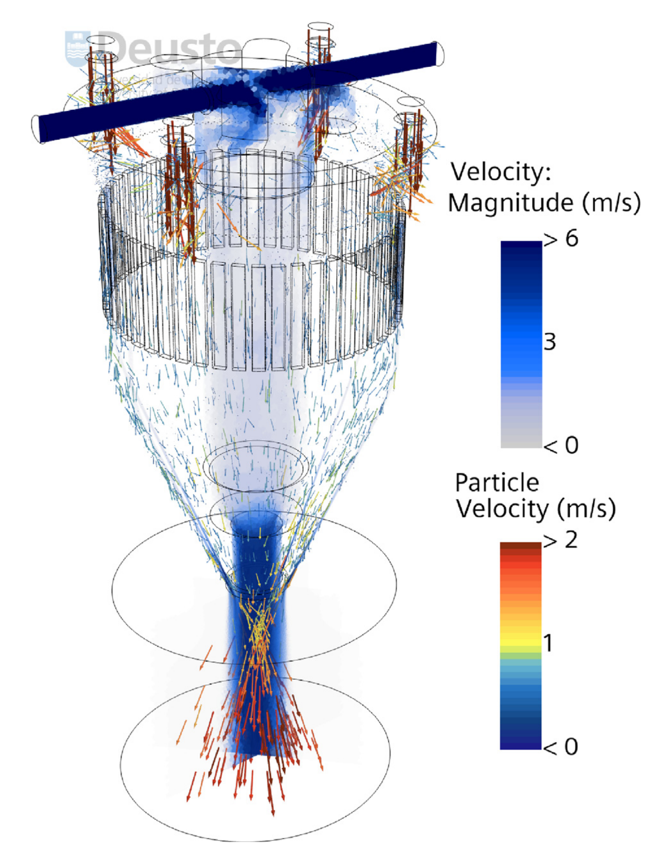

Fig. 5. Instantaneous particle velocity vectors in the converging section and at the nozzle exit, colored by velocity magnitude. The alignment imposed by the converging annulus and the acceleration imparted by the merging shielding stream are visible.

the distributor, particles arrive from the four conveying pipes with large tangential velocity components and undergo repeated oblique wall impacts; each rebound redistributes momentum between axial and lateral directions, producing the wide velocity spread visible in the percentile bands. The distributor fins then act as momentum filters: within the narrow fin channels the gas velocity rises locally (the secondary acceleration near $z \approx -70$ mm), particles are forced to align with the channel axis, and the lateral velocity variance collapses. On leaving the fins, the local gas deceleration in the wider annulus transfers energy back from the particles to the gas shear layer, explaining the deceleration feature. In the converging throat, the continuous area reduction accelerates the gas and, through drag, the particles—monotonically narrowing the stream. Finally, at the exit, the merger with the faster annular shielding stream provides the last and strongest acceleration impulse, which sets the exit velocity and, together with the geometric convergence angle, the standoff. Each mechanism thus leaves a distinct signature in Fig. 4, and their sequence—rebound dispersion → fin collimation → throat acceleration → shielding-jet boost—constitutes the causal chain from geometry to powder-stream focusing.

3.3. Mass flowrate estimation and flow irregularities

The instantaneous powder mass flowrate at the exit, $\dot{m}(t)$, is recorded throughout the transient simulation using a method analogous to the experimental workflow [24]. The flowrate is computed within a 1 mm thick slice located downstream of the nozzle exit. At each discrete time step k, the mass flowrate is calculated as:

$$\dot{m}_k = \sum_{i=1}^{N} \frac{m_i \cdot v_i}{\Delta z}, \tag{15}$$

where m_i is the mass of particle i, v_i is its axial velocity, and Δz is the slice thickness.

To characterize temporal fluctuations while filtering high-frequency noise, we apply a centered moving average with a 2 ms window:

$$\dot{m}_{k,\text{smoothed}} = \frac{1}{w} \sum_{j=-\lfloor w/2 \rfloor}^{\lfloor w/2 \rfloor} \dot{m}_{k+j}, \tag{16}$$

where w is the window size (number of time steps). This window length is chosen to retain physically meaningful pulsations (e.g., from particle rebounding and distributor-fin flow redistribution) while smoothing sub-millisecond stochastic variations.

We quantify the irregularity via the root-mean-square (RMS) percentage deviation of the flowrate from its temporal mean:

$$\overline{\dot{m}} = \frac{1}{T}\sum_{k=1}^{T}\dot{m}_k, \tag{17}$$

$$\mathrm{RMS}_{\dot{m}} = \sqrt{\frac{1}{T}\sum_{k=1}^{T}\left(\frac{\dot{m}_k - \overline{\dot{m}}}{\overline{\dot{m}}}\right)^2} \times 100\%, \tag{18}$$

where T is the total number of time steps over the statistically steady portion of the simulation (after initial transients decay). The resulting irregularity index is $\mathrm{RMS}_{\dot{m}} = 19\%$ (Fig. 6), consistent with the experimental trend of 16% [24], indicating that the model captures the dominant sources of unsteadiness: azimuthal flow redistribution at the distributor fins and rebound-driven intermittency near walls. Flow irregularities of this magnitude can affect deposition quality, particularly in high-speed printing or when dealing with small melt pools that are sensitive to rapid flow oscillations.

The contact treatment is directly implicated in this metric. The pulsation arises from two mechanisms that both depend on particle–wall interaction: (i) particles rebounding in the turning chamber and at the cone walls arrive at the exit in intermittent clusters rather than as a steady stream, with the restitution coefficient e setting how many rebounds a particle undergoes before alignment; and (ii) the JKR adhesion term allows slow particles to dwell briefly on fin and wall surfaces before re-entrainment, spreading residence times and adding low-frequency content to $\dot{m}(t)$. Purely elastic contact treatments, as adopted in most published nozzle simulations [6,8,10], cannot reproduce the second mechanism and generally report only time-averaged powder concentration fields, without quantifying delivery irregularity. The close match of the temporal irregularity index obtained here (19% vs. 16%) therefore constitutes indirect evidence that the adhesive contact treatment, with the independently measured surface energy [30], captures the wall-interaction physics relevant to the temporal structure of the delivered powder flow. A formal one-to-one comparison of identical simulations with and without adhesion would isolate the contribution of Γ_{12} quantitatively; this sensitivity study is planned as future work.

3.4. Limitations and sensitivities

The present CFD–DEM framework successfully captures dominant powder-flow trends, yet several modeling assumptions warrant discussion. **(i) Exit compressibility:** The incompressible RANS formulation underestimates gas expansion at the exit (local Mach ≈0.1–0.3), likely contributing to standoff underprediction (10.2 mm vs. 16 mm experimental); compressible RANS treatment in the exit region is recommended. **(ii) Drag calibration:** The Gidaspow correlation, while accounting for volume fraction effects, may require tuning for polydisperse, particle-laden jets; clustering and wake effects can modify the effective drag by 10–30% [15], and targeted calibration against experimental velocities could improve standoff accuracy. **(iii) DEM contact parameters:** Surface energy ($\Gamma_{12} = 0.01$ J/m^2) and friction ($\mu = 0.62$) are reasonable estimates but remain adjustable. **(iv) Mesh and near-wall treatment:** The polyhedral mesh with All-y^+ treatment trades near-wall detail for DEM coupling stability; wall-resolved LES would better capture fine-scale interactions at higher cost. **(v) Simplified PSD:** The coarser simulation PSD ($d_0 = 120\,\mu$m vs. 63.65 μm experimental) reduces computational demand but may underestimate fine-particle effects on cohesion and dispersion. **(vi) Turbulence dispersion:** RANS gradient diffusion may underestimate lateral spread of fine particles; stochastic or LES/DES approaches could improve footprint prediction for sub-100 μm sizes. **(vii) Mesh independence:** a formal multi-resolution independence study was not affordable for the coupled transient runs; mesh adequacy rests on targeted refinement of the highest-gradient regions, quality metrics, and validation of integral outputs, and a two-level comparison of exit velocity and standoff remains a recommended verification step. **(viii) Single operating point:** validation is restricted to the fully characterized operating condition of the companion experimental study [24]; predictive capability across gas-flow splits, feed rates, and geometries remains to be demonstrated.

3.5. Transferability and applicability

The simulation methodology is directly transferable to other gas-conveyed particulate systems where temporal flow characteristics and spatial distributions are critical, including alternative LMD nozzle designs, directed energy deposition with different energy sources, thermal spray processes, powder bed fusion with

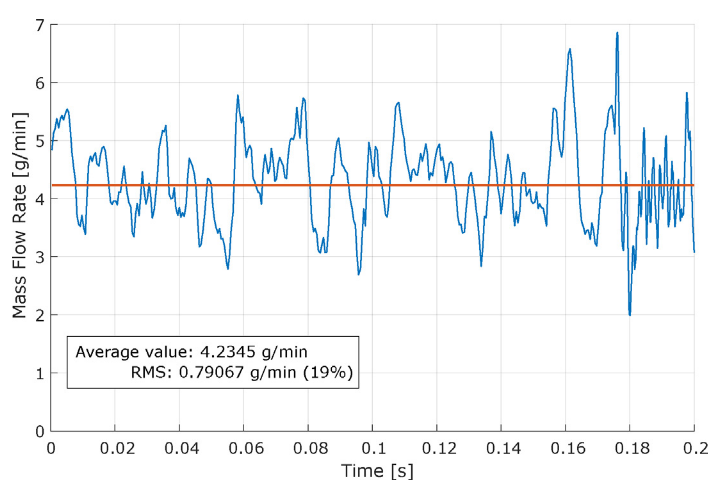

Fig. 6. Simulated powder mass flowrate over time: 2 ms moving-average signal $\dot{m}_{k,\mathrm{smoothed}}$ (blue), consistent with the experimental filtering procedure [24], and its temporal mean $\overline{\dot{m}}$ (orange).

gas-jet delivery, and pharmaceutical powder dispensing. Adapting the framework requires calibration of DEM contact parameters (Γ_{12}, μ, e) and drag models for different powder materials, while compressible flow treatment becomes necessary for higher Mach numbers exceeding 0.3. Dense loading scenarios with $\epsilon_g < 0.8$ benefit from the Gidaspow model's automatic Ergun transition, though additional subgrid closures may be needed for four-way coupling.

Practitioners should verify mesh quality metrics match those reported here, conduct geometry-specific independence studies, establish mass conservation within 1% before collecting statistics, and validate at least two independent metrics against experimental data. The computational cost scales linearly with particle count in the dilute regime: at 560 core-hours per second of physical time, a 10-point design sweep requires about 3000 core-hours, accessible with modest HPC resources.

4. Conclusion

A coupled CFD–DEM model of a continuous coaxial LMD nozzle, combining a polyhedral mesh, SST k–ω turbulence, Gidaspow drag, and a JKR-type adhesive contact implemented via field functions in STAR-CCM+, was compared against companion experimental data at a fully characterized operating point [24]. The core quantitative findings are:

1. **Validated — temporal flow stability:** the predicted exit mass-flow irregularity of 19% (2 ms moving-average RMS) closely matches the experimental 16%, and is mechanistically linked to particle rebound intermittency and azimuthal redistribution at the distributor fins, both enabled by the DEM contact treatment with independently measured surface energy [30].
2. **Validated — particle dynamics:** peak particle accelerations of $\approx$50 m/s^2 at the throat/exit reproduce the experimentally inferred order of magnitude, supporting the Gidaspow drag and Sommerfeld lift closures in this dilute regime, and the simulation resolves the full causal chain of rebound dispersion, fin collimation, throat acceleration, and shielding-jet boost.
3. **Not yet validated — standoff distance:** the simulated 10.2 mm underpredicts the experimental 16 mm; a ballistic estimate indicates that the incompressible treatment of the exit expansion ($Ma \approx 0.1$–0.3) and the coarser simulation PSD ($\sim$3.5$\times$ longer particle response time) act in the same direction and are consistent with the discrepancy. Compressible exit-region treatment and a PSD-matched rerun are the corresponding model improvements still required.
4. **Methodology:** the automated extraction of percentile-based standoff, footprint statistics, centerline velocity/acceleration profiles, and time-resolved mass-flow irregularity from the transient solution provides a reproducible performance-assessment framework at a documented cost of $\sim$560 core-hours per second of physical time.

Remaining assumptions that require future verification include the single-mesh resolution, the single validated operating point, and the sensitivity of the results to the DEM contact parameters; these are detailed in SubSection 3.4.

Ethics statements

This work does not have any outstanding ethical implications.

Declaration of generative AI and AI-assisted technologies in the manuscript preparation process

During the preparation of this work, the authors used GitHub Copilot in order to assist with code formatting, reference checking, LaTeX syntax corrections, and manuscript structure review. After using these tools, the authors reviewed and edited the content as needed and take full responsibility for the content of the published article.

CRediT authorship contribution statement

Lorenzo Pedrolli: Writing – original draft, Visualization, Validation, Software, Project administration, Methodology, Investigation, Formal analysis, Data curation, Conceptualization.**Alejandro Lopez**: Writing – review & editing, Supervision, Resources, Funding acquisition.**Beatriz Achiaga**: Writing – review & editing, Supervision, Resources, Conceptualization.

Declaration of competing interest

The authors declare that they have no known competing financial interests or personal relationships that could have appeared to influence the work reported in this paper.

Acknowledgements

This study received financial support from the Basque Government through the Research Group program IT1507-22.

This project has received funding from the European Union's Horizon 2020 research and innovation programme under the Marie Skłodowska-Curie grant agreement No. 847624. In addition, a number of institutions back and co-finance this project. The content of this work reflects only the author's view, the Agency is not responsible for any use that may be made of the information it contains.

Appendix A. Supplementary data

Supplementary data associated with this article can be found, in the online version, at https://doi.org/10.1016/j.apt.2026.105403.

References

[1] D.-G. Ahn, Directed energy deposition (DED) process: state of the art, Int. J. Precis. Eng. Manuf.-Green Technol. 8 (2) (2021) 703–742. https://doi.org/10.1007/s40684-020-00302-7.
[2] D.R. Feenstra, R. Banerjee, H.L. Fraser, A. Huang, A. Molotnikov, N. Birbilis, Critical review of the state of the art in multi-material fabrication via directed energy deposition, Curr. Opin. Solid State Mater. Sci. 25 (4) (2021) 100924. https://doi.org/10.1016/j.cossms.2021.100924, URL https://www.sciencedirect.com/science/article/pii/S1359028621000279.
[3] A. Singh, S. Kapil, M. Das, A comprehensive review of the methods and mechanisms for powder feedstock handling in directed energy deposition, Addit. Manuf. 35 (2020) 101388. https://doi.org/10.1016/j.addma.2020.101388, URL https://www.sciencedirect.com/science/article/pii/S2214860420307600.
[4] J.I. Arrizubieta, I. Tabernero, J.E. Ruiz, A. Lamikiz, S. Martinez, E. Ukar, Continuous coaxial nozzle design for LMD based on numerical simulation, Phys. Proc. 56 (2014) 429–438. https://doi.org/10.1016/j.phpro.2014.08.146, URL https://www.sciencedirect.com/science/article/pii/S1875389214002910.
[5] A. López-Martínez, J. Ibarra-Medina, A.-I. García-Moreno, S. Piedra, L. del Llano Vizcaya, E. Martínez-Franco, M. Megahed, Modeling and comparison of the powder flow dynamics for tilted annular and discrete-outlet nozzles in laser directed energy deposition, J. Manuf. Process. 99 (2023) 687–704. https://doi.org/10.1016/j.jmapro.2023.05.039, URL https://www.sciencedirect.com/science/article/pii/S1526612523005017.
[6] I. Tabernero, A. Lamikiz, E. Ukar, L.N. López de Lacalle, C. Angulo, G. Urbikain, Numerical simulation and experimental validation of powder flux distribution in coaxial laser cladding, J. Mater. Process. Technol. 210 (15) (2010) 2125–2134. https://doi.org/10.1016/j.jmatprotec.2010.07.036.
[7] M. Ostolaza, A. Urresti, J.I. Arrizubieta, A. Lamikiz, M. Ortiz, Cfd simulation for the modelling of the powder flow on continuous coaxial nozzles in the laser ded process, Procedia CIRP 111 (2022) 282–286, 12th CIRP Conference on Photonic Technologies [LANE 2022]. doi:10.1016/j.procir.2022.08.022.
[8] J. Gao, C. Wu, X. Liang, Y. Hao, K. Zhao, Numerical simulation and experimental investigation of the influence of process parameters on gas-powder flow in laser metal deposition, Opt. Laser Technol. 125 (2020) 106009. https://doi.org/10.1016/j.optlastec.2019.106009.
[9] X. Guan, Y. Zhao, Modeling of the laser powder–based directed energy deposition process for additive manufacturing: a review, Int. J. Adv. Manuf. Technol. 107 (2020). https://doi.org/10.1007/s00170-020-05027-0, Mar..

[10] X. Gao, X.X. Yao, F.Y. Niu, Z. Zhang, The influence of nozzle geometry on powder flow behaviors in directed energy deposition additive manufacturing, Adv. Powder Technol. 33 (3) (2022) 103487. https://doi.org/10.1016/j.apt.2022.103487, URL https://www.sciencedirect.com/science/article/pii/S0921883122000656.

[11] D. Mukin, N. Larionov, E. Valaytseva, G. Turichin, Powder particle transport in direct laser deposition: Modeling a gas-powder flow formed by a single nozzle tube, Powder Technol. 470 (2026) 121907. https://doi.org/10.1016/j.powtec.2025.121907.

[12] J. Qin, P. Jing, Y. Li, H. Zhu, S. Zhong, L. Zhang, Spatial dynamic characteristics of powder stream and particles during laser cladding with coaxial powder feeding, J. Manuf. Sci. Eng. 148 (5) (2026). https://doi.org/10.1115/1.4071095, Mar.

[13] L. Zhang, Z. Zhang, Particle motion control in ultrasonic assisted directed energy deposition, Int. J. Mech. Sci. 294 (2025) 110259. https://doi.org/10.1016/j.ijmecsci.2025.110259.

[14] C.T. Crowe, J.D. Schwarzkopf, M. Sommerfeld, Y. Tsuji, Multiphase Flows with Droplets and Particles, 2nd Edition., Taylor and Francis Ltd., Boca Raton, FL, 2011, URL https://www.ebook.de/de/product/21177407/clayton_t_crowe_john_d_schwarzkopf_martin_sommerfeld_yutaka_tsuji_multiphase_flows_with_droplets_and_particles.html.

[15] M. Sommerfeld, Numerical methods for dispersed multiphase flows, in: Advances in Mathematical Fluid Mechanics, Springer International Publishing, 2017, pp. 327–396. doi:10.1007/978-3-319-60282-0_6.

[16] R. Stanly, G. Shoev, Detailed analysis of recent drag models using multiple cases of mono-disperse fluidized beds with Geldart-B and Geldart-D particles, Chem. Eng. Sci. 188 (2018) 132–149. https://doi.org/10.1016/j.ces.2018.05.030, URL https://www.sciencedirect.com/science/article/pii/S0009250918303270.

[17] P.J. O'Rourke, P.P. Zhao, D. Snider, A model for collisional exchange in gas/liquid/solid fluidized beds, Chem. Eng. Sci. 64 (8) (2009) 1784–1797. https://doi.org/10.1016/j.ces.2008.12.014, URL https://www.sciencedirect.com/science/article/pii/S0009250908006829.

[18] S. Kuang, M. Zhou, A. Yu, CFD-DEM modelling and simulation of pneumatic conveying: a review, Powder Technol. 365 (2020) 186–207. https://doi.org/10.1016/j.powtec.2019.02.011, URL https://www.sciencedirect.com/science/article/pii/S003259101930107X.

[19] L. Pedrolli, B. Achiaga Menor, I. Martinez de Arenaza, A. López, Comparison of cfd-dem and mp-pic in the simulation of metal powder conveying for laser metal deposition, OpenFOAM® J. 4 (2024) 26–40. https://doi.org/10.51560/ofj.v4.91.

[20] J. Wang, P. Zhao, B. Zhao, Testing CFD-DEM method with a stochastic drag formulation using particle-resolved direct numerical simulation data as benchmark, Chem. Eng. Sci. 240 (2021) 116657. https://doi.org/10.1016/j.ces.2021.116657, wOS:000656201400002. https://gateway.webofknowledge.com/gateway/Gateway.cgi?GWVersion=2&SrcAuth=DynamicDOIArticle&SrcApp=UA& KeyAID=10.1016%2Fj.ces.2021.116657&DestApp=DOI& SrcAppSID= E4TWsCm86ubcwchnxC2& SrcJTitle=CHEMICAL+ENGINEERING+SCIENCE&DestDOIRegistrantName=Elsevier.

[21] J. Tomas, Adhesion of ultrafine particles - a micromechanical approach, Chem. Eng. Sci. 62 (7) (2007) 1997–2010. https://doi.org/10.1016/j.ces.2006.12.055, URL https://www.sciencedirect.com/science/article/pii/S0009250907000073.

[22] C. Thornton, Z. Ning, A theoretical model for the stick/bounce behaviour of adhesive, elastic-plastic spheres, Powder Technol. 99 (2) (1998) 154–162. https://doi.org/10.1016/S0032-5910(98)00099-0, URL https://www.sciencedirect.com/science/article/pii/S0032591098000990.

[23] M. Pasha, S. Dogbe, C. Hare, A. Hassanpour, M. Ghadiri, A linear model of elasto-plastic and adhesive contact deformation, Granular Matter 16 (1) (2014) 151–162. https://doi.org/10.1007/s10035-013-0476-y.

[24] L. Pedrolli, J.I. Arrizubieta Arrate, G. Bonifazi, A. Lamikiz, B. Achiaga, A. Lopez, Experimental analysis of the powder flow in a continuous coaxial nozzle for laser metal deposition, Progress in Additive Manufacturing 11 (4) (2026) 4477–4495. doi:10.1007/s40964-026-01600-3. https://link.springer.com/10.1007/s40964-026-01600-3.

[25] M.L. Thomas, P.W. Longest, Evaluation of the polyhedral mesh style for predicting aerosol deposition in representative models of the conducting airways, J. Aerosol Sci. 159 (2022) 105851. https://doi.org/10.1016/j.jaerosci.2021.105851.

[26] F.R. Menter, Two-equation eddy-viscosity turbulence models for engineering applications, AIAA J. 32 (8) (1994) 1598–1605. https://doi.org/10.2514/3.12149.

[27] D. Gidaspow, Multiphase flow and fluidization: continuum and kinetic theory descriptions, Academic Press, Boston, 1994.

[28] L. Pedrolli, L. Fraccarollo, B. Achiaga, A. Lopez, Optical particle tracking in the pneumatic conveying of metal powders through a thin capillary pipe, Technologies 12 (10) (2024) 191. https://doi.org/10.3390/technologies12100191.

[29] K.L. Johnson, A.K. Kendalland, D. Roberts, Surface energy and the contact of elastic solids, Proceedings of the Royal Society of London. A. Mathematical and Physical Sciences 324 (1558) (1971) 301–313. doi:10.1098/rspa.1971.0141.

[30] L. Pedrolli, S. Nadimi, B. Achiaga, A. López, Estimation of mesoscale surface energy in the kinetic adhesion test, Powder Technol. 435 (2024) 119426. https://doi.org/10.1016/j.powtec.2024.119426.

[31] K. Odum, M. Soshi, K. Yamazaki, Measurement and analysis of impact dynamics suitable for modelling pneumatic transport of metallic powder flow through a directed energy deposition nozzle, Adv. Powder Technol. 33 (3) (2022) 103515. https://doi.org/10.1016/j.apt.2022.103515, URL https://www.sciencedirect.com/science/article/pii/S0921883122000930.

[32] T. Roessler, C. Richter, A. Katterfeld, F. Will, Development of a standard calibration procedure for the dem parameters of cohesionless bulk materials – part i: Solving the problem of ambiguous parameter combinations, Powder Technol. 343 (2019) 803–812. https://doi.org/10.1016/j.powtec.2018.11.034.

[33] C. Richter, T. Rößler, G. Kunze, A. Katterfeld, F. Will, Development of a standard calibration procedure for the dem parameters of cohesionless bulk materials – part ii: Efficient optimization-based calibration, Powder Technol. 360 (2020) 967–976. https://doi.org/10.1016/j.powtec.2019.10.052.